UNIVERSITY OF CALIFORNIA,
IRVINE

Effect of Water Vapor on Grain-Boundary Diffusion of Oxygen in Ceramic Processing

THESIS

submitted in partial satisfaction of the requirements
for the degree of

MASTER OF SCIENCE

in Materials Science and Engineering

by

Michael Lu

Thesis Committee:
Professor Martha Mecartney, Chair
Professor James Earthman
Professor Regina Ragan

2016

TABLE OF CONTENTS

LIST OF FIGURES

LIST OF TABLES

ACKNOWLEDGMENTS

First of all, I would like to express my deepest gratitude to my committee chair and advisor, Professor Martha Mecartney, for her constructive advices, useful critiques, and continuous support for my work. My accomplishment would not be possible without her guidance and resource.

My appreciation also goes to the entire Mecartney's lab group: Austin Travis, Kenta Ohtaki, David Kok, and Joanne Leadbetter. The lab will not be fun without you guys around. Special thanks to Austin Travis for his mentoring and assistance when I first stepped into Mecartney's lab, and to Kenta Ohtaki, for his mechanic skills to fix anything!

In addition, I would like to thank my undergraduate squad for their contributions to this project: Salah Ezzeldin Abdelrahman Moh Saad, Victor Hugo Jr. Cobar, and Dania Alfeerawi. I now deem you as Master of Polishing.

Last but not least, I would also like to thank NSF DMR 1243898 for the funding and The Laboratory for Electron and X-ray Instrumentation (LEXI) for providing access to use the state-of-the-art facility. None of my materials characterization would be possible without the use of SEM and XRD.

Permissions for using copyrighted figures are granted by Copyright Clearance Center and John Wiley and Sons.

ABSTRACT OF THE THESIS

Effect of Water Vapor on Grain-Boundary Diffusion of Oxygen in Ceramic Processing

By

Michael D. Lu

Master of Science in Materials Science and Engineering

University of California, Irvine, 2016

Professor Martha Mecartney, Chair

The results of prior experiments have suggested faster diffusion of oxygen in polycrystalline alumina when exposed to water vapor. It is hypothesized that the dissociation of water vapor on the oxide surface helps increase the transport of oxygen in the form of the smaller hydroxide ion through grain-boundary diffusion. This study examines the sintering of ceramics and the oxidation of nickel in an 8YSZ/0.5 vol.% nickel cermet. In YSZ oxygen anion diffusion is fastest in grains due to the spaces in the fluorite unit cell and yttrium cations creating oxygen vacancies. Oxygen diffusion along grain boundaries in YSZ is actually slower than in the grains. In the first part of the study, ceramics are sintered at temperatures of 1000-1500°C for 3 hours in dry air or humid air (0.2 atm P_{water}). Percent theoretical densities of sintered α-alumina, spinel and 8YSZ sintered in the two atmospheres at various sintering temperatures will be plotted and compared. In the second part of the study, polished surfaces of 8YSZ-Ni cermet are exposed to dry air or humid air (0.38 atm P_{water}) at temperatures of 1000°C for times from 30 minutes to 2 hours. Preliminary data on the parabolic oxidation kinetics found that the oxidation depth for Ni^0 → Ni^{2+} increased in the presence of humid air. The kinetic rate constants of oxygen diffusion

calculated from oxidation depth of nickel front under dry and humid conditions at high temperatures will be reported.

CHAPTER 1: INTRODUCTION

Atmosphere plays an important role in defining how we design or choose materials for their application. Majority of the materials are exposed to some extent of humidity in their applications. The introduction of humidity is unwelcoming, as metals corrode faster in humid environments [1]. The deterioration leads to change in materials' mechanical properties and often causes material failures. Oxide ceramic materials, on the other hand, are thought of as having already been oxidized so they are generally resistant to environmental degradation. Therefore, they are widely used for applications that operate in extreme environments in air or oxidizing atmospheres.

Even as very stable materials, ceramic materials can degrade when exposed to water. Numerous literatures have shown that under high-temperature water vapor, ceramics can experience phase transformation, exacerbated grain growth, and faster densification [2-11]. Even though the driving forces for these phenomena are different, they all require some sort of diffusion, and many researchers have hypothesized that it is the diffusion of oxygen in the form of hydroxyl ions (OH^-) that result in these phenomena. Water dissociates readily onto oxide surfaces, and the dissociation mechanism of water in YSZ is depicted in Fig. 1.1. Using Kroeger-Vink notation, the water dissociation can be described as the following:

$$2Y'_{Zr} + V_{\ddot{O}} + H_2O(g) + 3O_O^x \xrightarrow{8YSZ} 2OH_{\dot{O}} + 2Y'_{Zr} + 2O_O^x$$

As water molecules dissociate, superficial oxygen vacancies are annihilated and replaced with OH^-, and the remaining protons, H^+, bond to nearby lattice oxygen to create more OH^- [12]. The ionic radius of OH^- and O^{2-} is 99pm and 126pm, respectively [6; 13]. Diffusivity of OH^- is believed to be higher than that of O^{2-} because OH^- has smaller ionic radius and reduced charge. Moreover,

where OH^- cannot diffuse further, proton hopping of hydrogen to adjacent lattice oxygen ion is possible for easier diffusion.

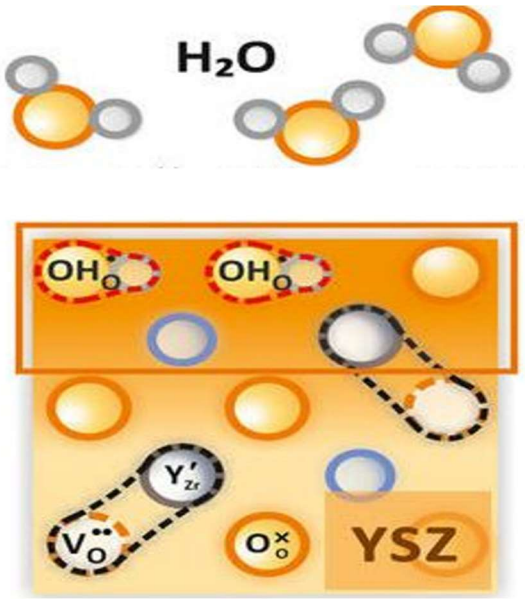

Figure 1.1: Dissociation mechanism of water at YSZ surface-gas interface [12]

Here, we are interested in the effects of water vapor on the densification of alumina, spinel and 8YSZ, and on the oxidation of Ni marker in 8YSZ. Both sintering and oxidation are grain-boundary diffusion-controlled, where oxygen diffusion is the rate-determining step. The goal for this work is to test the hypothesis that water vapor will enhance the diffusion-controlled processes in oxides where grain-boundary diffusion of O^{2-} in the form of OH^- is the primary mechanism.

CHAPTER 2: EXPERIMENTAL PROCEDURES

Information about the materials used in the studies is listed in Table 2.1. Processing and characterization of these materials are described in this chapter.

Table 2.1: Information on the starting powders used in the studies

Starting Powder	Vendor	Density (g/cm^3)	Starting Particle Size (nm)	Crystal Structure
Baikowski Alumina (α-Al_2O_3)	Baikowski	3.97	600	Hexagonal
Taimei Alumina (α-Al_2O_3)	Taimei	3.97	150	Hexagonal
Mg-Spinel ($MgAl_2O_4$)	Baikowski	3.58	200	Cubic
8 mol% Yttria-Stabilized Zirconia (8YSZ)	Tosoh	5.90	50	Cubic
NiO	Alfar Aesar	6.67	200	Cubic

2.1 Materials Synthesis and Sample Preparation

2.1.1 Wet Attrition Milling

The first step for ceramic powder processing is usually attrition milling of the powder to attain smaller and finer starting particle size and/or homogeneous mixing of two or more materials. Feeding material (ceramic powder), grinding media (YTZ beads) and a liquid (isopropanol) make up the main components of wet attrition milling. The crushing and shearing of the powder from the interaction between the powder and grinding media is activated by the rotation of agitator shaft and facilitated by isopropanol. The advantages of having wet attrition milling also include better dispersion of the powder and reduction of heat generation. To prevent contamination, YTZ milling media was chosen because it has superior wear resistance. Here, the powders were milled using a Union Process attritor mill.

2.1.2 Ball Milling

Ball milling is a much more cost-saving way of mixing two or more ceramic powders and breaking up agglomerates present in the powders from the manufacturer's packages. In the study of oxidation of nickel particles in 8YSZ, ball milling was used to assure that the nickel marker is evenly distributed in the 8YSZ matrix.

2.1.3 Cold Isostatic Press

Pressing the powder is often necessary for sintering, as high sintered density can be achieved at relatively lower sintering temperature and shorter time for higher green body's density, also known as green density. Cold isostatic press (CIP) applies fluid medium to uniformly press powder into a compact. The shape of the green body is defined by the shape that silicone mold makes, which was cylindrical. The powder was packed inside the silicone mold, before the lid was placed and sealed using tape. Then, the mold was placed into a balloon, and the balloon was vacuumed and sealed. It was then pressed in the CIP at 55kpsi for 5 minutes The green density was measured using geometric method, which will be described in the later section. Typically, the green density came out between 50-57% dense.

2.1.4 Furnace Operation

Sintering, reduction and oxidation in high temperature were done using Lindberg/Blue M 1500ºC General Purpose Tube Furnace accommodated with SiC heating elements and PID programmable control. For the purpose of this study where different atmospheres were run, gas tanks of 4% H_2-Ar and ultra-pure zero grade compressed air were attached to the tube furnace with a mass flow controller (MFC) that can control the flow rate during furnace operation. The setup is illustrated in Fig. 2.1.

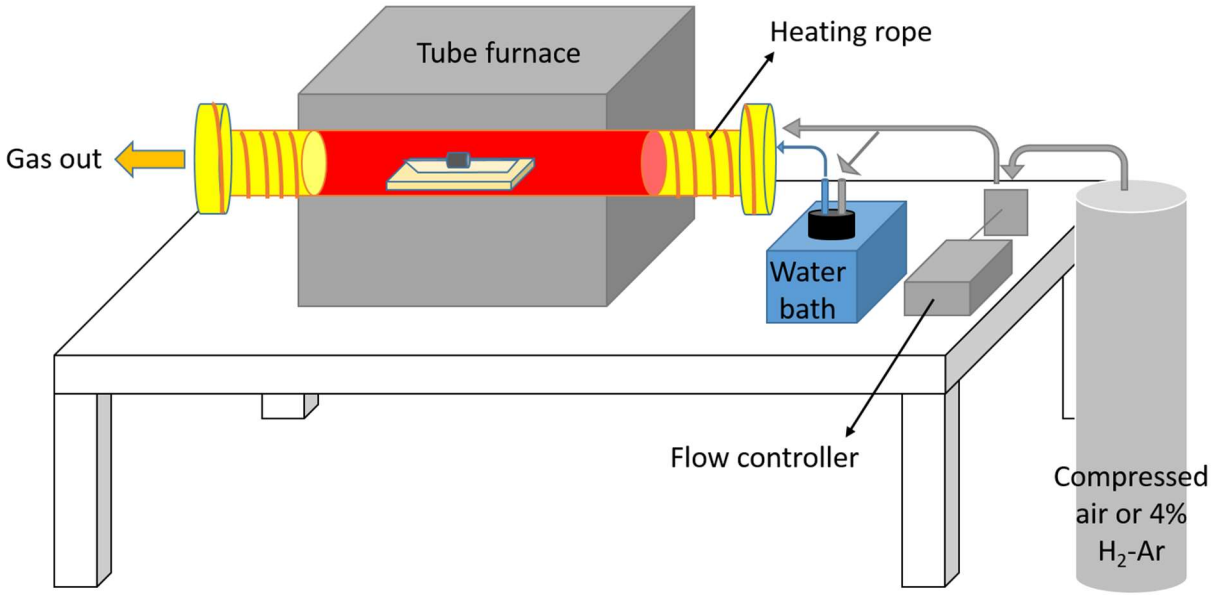

Figure 2.1: Schematic of the tube furnace setup

A layer of powder, which is the same material as the pressed specimens, was first transferred to cover the bottom of alumina combustion boat. Then, the pressed specimens were placed on top of the powder bedding, and the combustion boat was loaded into the tube furnace. A heating profile was entered and adjusted based on the studies, and a general heating profile is depicted in Fig. 2.2. A holding temperature of 300ºC for some time was used to ensure that the system was flushed with the required atmospheres before ramping up the temperature. Cooling was done by convection cooling.

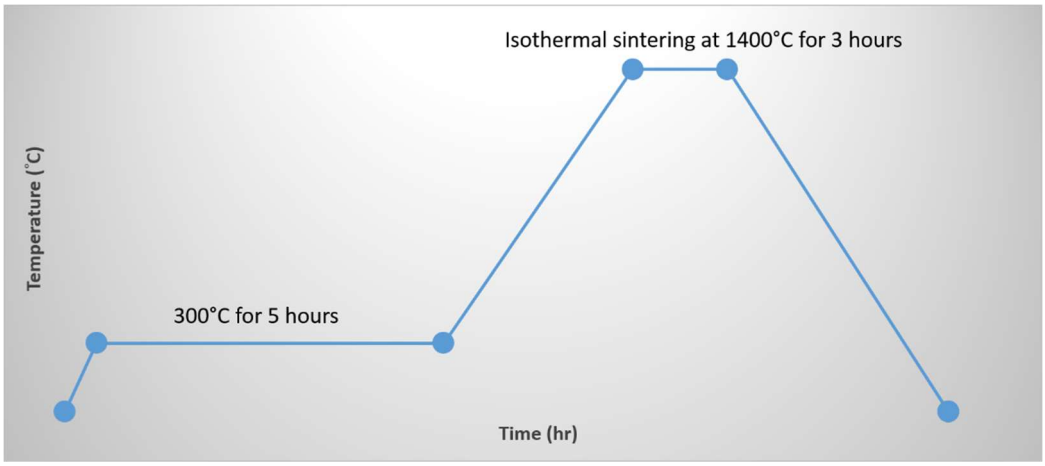

Figure 2.2: A general heating profile for sintering of oxides

2.1.5 Humid Environment Run

To introduce water vapor into the system during oxidation and sintering, a water bath was set up as depicted in Fig. 2.1. The compressed air was flowed through a flask of deionized water placed in a water bath, and then the humidified air would flow into the tube furnace. Shown in Fig. 2.3, desired partial pressure of water vapor can be reached and maintained by adjusting the water bath temperature. The use of heating rope at a temperature of 190ºC around the tube was to prevent the condensation of water vapor on the part of the tube that was not exposed to the hot zone in the furnace.

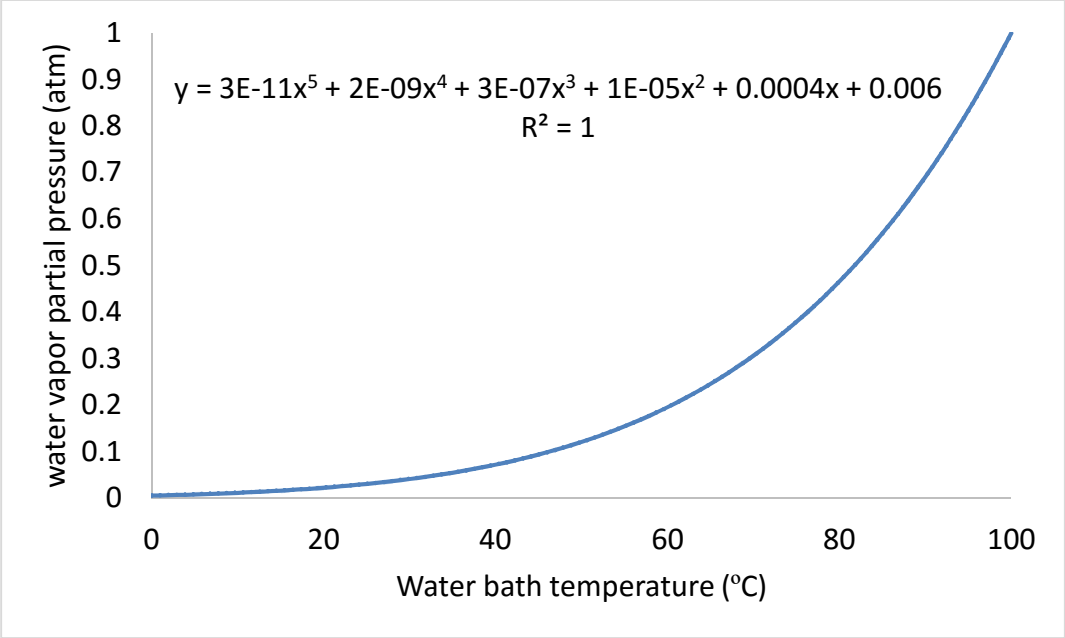

Figure 2.3: Water vapor partial pressure as a function of water bath temperature

2.1.6 Ceramography

The typical steps for ceramic specimens for microstructural analysis are cutting, grinding, polishing, and sometimes, etching. Ceramography is crucial for failure analysis of ceramic materials in technological companies.

In the oxidation study, oxidized specimens were first glued to a metal plate using crystal bond, and then the metal plate was fixed onto the stage of precision diamond saw for cutting the specimens into rectangular cross section with a thickness of 1-1.5 mm. A simple diagram is drawn for cutting of an oxidized specimen (Fig. 2.4). After cutting, the specimens were place in a beaker of acetone and sonicated to dissolve the crystal bond from the specimens.

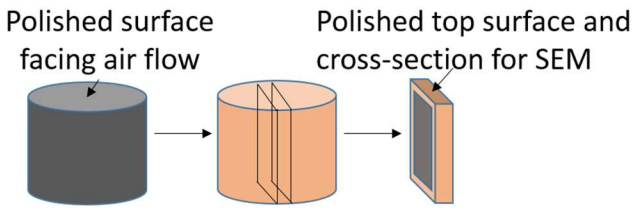

Figure 2.4: A flow chart showing the cutting of a specimen after being oxidized

The cross-sectioned specimens had a rough surface after cutting, so grinding the specimens to flat surface was necessary before moving on to polishing. The specimens were smoothed using 240-grit SiC grinding paper on a Buehler Variable Speed Grinder-Polisher. Then, the flat specimens were polished with diamond lapping films from 30 microns down to 0.1 micron. By using an optical microscope, the specimens were inspected after each step of polishing to ensure that the specimens were free of scratches for SEM analysis.

In order to reveal that nickel is sitting on the grain boundary under SEM, polished cross-sectioned specimens had to be thermally etched using the tube furnace. The specimens were loaded into the furnace, and hydrogen gas was flushed into the tube for 5 hours before the heating profile was initiated. Thermal etch was performed at 1350ºC for 30 minutes with a ramp rate of 35ºC/minute.

2.1.7 Sputter Coating

SEM imaging of ceramic specimens requires the specimens to be coated with metal, as ceramics are not electrically conductive and will charge up under SEM if not coated. Here, the specimens were coated with Iridium under 8kV and 3mA for 10 minutes (South Bay Technology Ion Beam Sputtering/ Etching System).

2.2 Materials Characterizations

2.2.1 Density Measurements

Both studies required accurate density measurement. Densities were measured to show difference in densification rate for the dry air vs. humid air for the sintering study. On the other hand, density consistency of 8YSZ-Ni specimens was crucial for oxidation study, as lower density would result in more open structure for oxygen to diffuse easier. Therefore, it was obligatory to carefully select and develop density measurement methods. Three methods were used: volumetric density measurement, density measurement by ASTM standards, and density measurement by nail polish coating.

Volumetric density measurement simply uses the geometry and dry weight of the specimen. The specimens in the studies were cylindrical, and the density can be calculated with Equation 1 and Equation 2,

$$V_{RC} = \pi r^2 h \quad (1)$$

$$\rho = \frac{M}{V_{RC}} \quad (2)$$

where V_{RC} is the volume of right cylinder, r is the radius of the cylinder, h is the height of the cylinder, ρ is the density, and M is the mass. This method was used mainly to measure the green body density, as the channels connecting the open pores and close pores in the green body render the other methods incompatible. However, because the specimens were not shaped to perfect right cylinders, a stricter method had to be implemented for sintered bodies.

Density measurement by nail polish coating was investigated. The nature of nail polish is hydrophobic, so it will not easily absorb water. Archimedes' density measurement of specimens coated with nail polish can therefore be applied with water as the suspending liquid. The dry weight of the specimen (W_{dry}) was first measured using an analytical digital balance, and nail polish was

then painted evenly to cover the specimen's surface. Once the nail polish dried up, the dry and suspended weights of the coated specimen were measured using hydrostatic setup on the digital balance. Bulk density of the specimen can then be approximated using Equation 3,

$$\rho_{bulk} = \frac{W_{dry}}{W_{DCS} - W_{SCS}} \times \rho_{water} \qquad (3)$$

where ρ_{water} is density of water, W_{DCS} is the weight of dry coated specimen, and W_{SCS} is the weight of suspended coated specimen. The approximation is based on the assumption that the volume of nail polish is negligible compared to the specimen's volume, so the volume of the coated specimen can be substituted for the specimen's bulk volume. The thickness of nail polish on the specimen was found to be about 75 microns. Based on this thickness value, a model of cylindrical specimen volume and nail polish volume required to entirely cover the specimen's surface was constructed (Fig. 2.5). The cylindrical specimen volume increases in cubic power, while the nail polish volume increases in the power of 2. With the specimen in the studies having a radius of roughly 3 mm, a 9.1% error for volume was calculated. Table 2.2 shows that the nail polish method would work better on a larger specimen, such as one with a radius of 10 mm (2.9% error).

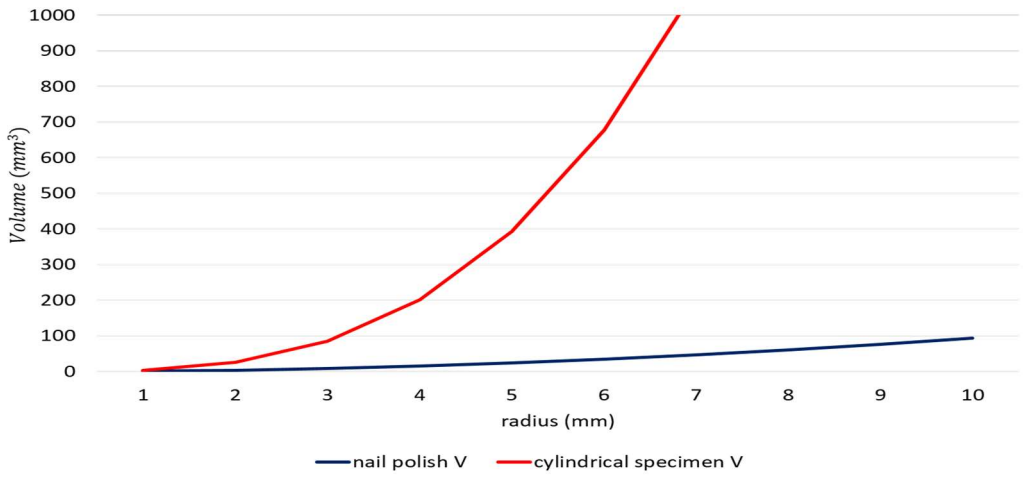

Figure 2.5: A simulated graph of cylindrical specimen volume and nail polish volume required to entirely cover the specimen's surface.

Table 2.2: Decreasing % error of nail polish coating method with increasing sample size

radius	% error
1	23.1
2	13.0
3	9.1
4	7.0
5	5.7
6	4.8
7	4.1
8	3.6
9	3.2
10	2.9

A much more ideal method, ASTM C20, was adopted for measuring density of sintered bodies with pores [14]. ASTM is a testing standard that has been followed by many industries all over the world. ASTM C20 is developed for measuring bulk density of refractory bricks, and it is a slight modification of Archimedes' principle (Fig. 2.6). Archimedes' principle does not take open pores into account, but ceramics are known to contain open pores when not sintered to nearly full density. The dry weight of the sintered specimen (W_{dry}) was measured, and the specimen was transferred into a beaker of deionized water. Then, the beaker was placed on a hot plate or in a vacuum chamber to draw air out of the open pores of the specimen and to allow the water to infiltrate into the open pores. Suspended weight (W_{susp}) was measured, and the specimen was dried lightly with a damp Kimwipe to prevent sucking the water out of the open pores. Lastly, saturated weight (W_{sat}) was measured, and the bulk density was calculated using Equation 4.

$$\rho_{bulk} = \frac{W_{dry}}{W_{sat} - W_{susp}} \times \rho_{water} \qquad (4)$$

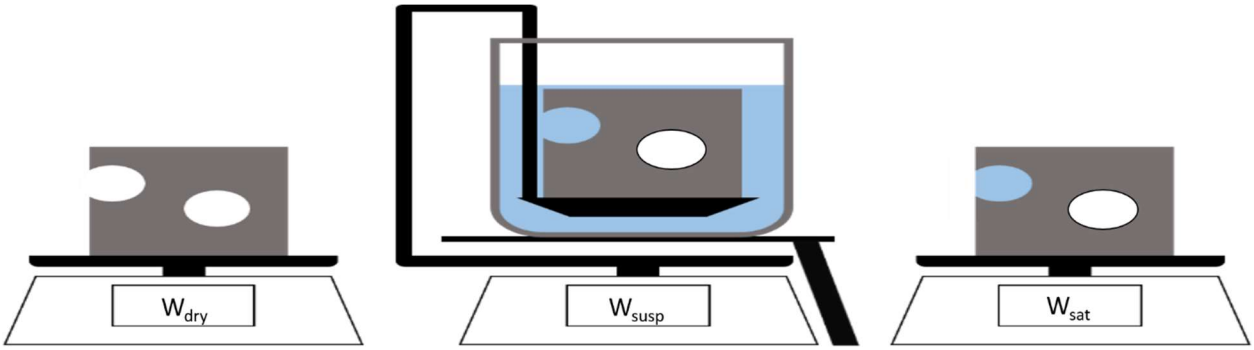

Figure 2.6: Illustration of ASTM C20 standard test methods

To calculate the relative density (% theoretical density) of a specimen, the following equation can be used:

$$\% \text{ theoretical density} = \frac{\rho_{specimen}}{\rho_{theoretical}} \qquad (5)$$

where $\rho_{specimen}$ is the measured density of the bulk specimen, and $\rho_{theoretical}$ is the theoretical density of the material.

Table 2.3 shows the summary of the three density measurements on four spinel specimens sintered at 1300ºC. Both volumetric and nail polish coating methods are underestimating the bulk density. Density measurement using nail polish coating method gives 7% error, which is close to the calculated error of 9.1% from Table 2.2.

Table 2.3: Comparison of sample's density with three different measurements

Ground Baikowski Spinel	Specimen	Air		
		% theo. Density using volumetric method	% theo. Density using ASTM C20 method	% theo. Density using nail polish coating method
1300°C	1	0.685	0.721	0.660
	2	0.710	0.726	0.681
	3	0.710	0.726	0.679
	4	0.685	0.715	0.665

2.2.2 X-Ray Diffraction (XRD)

XRD analysis can reveal information about phases in a crystalline material as well as the dimension of the unit cell for the identified phases. The concept behind XRD is Bragg's Law (Equation 6), where constructive interferences resulted from the interaction between a monochromatic X-ray and crystalline phase will create a peak pattern that is unique to each crystalline phase (Fig. 2.7). λ is the wavelength of the radiation, n is a positive integer, d_{hkl} is the d-spacing corresponding to a specific hkl plane, and θ is the angle.

$$n\lambda = 2d_{hkl} \cdot sin\theta \qquad (6)$$

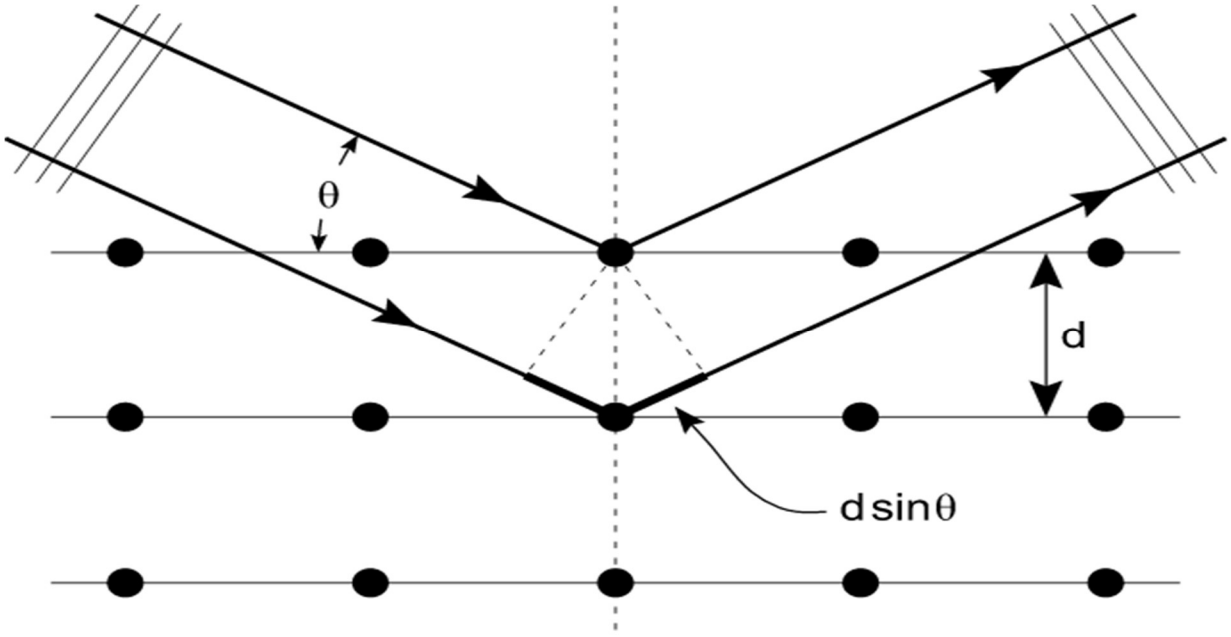

Figure 2.7: Bragg diffraction

Rigaku SmartLab X-ray Diffractometer (Tokyo, Japan) was used to identify and verify the phases by using Cu-K_α radiation (λ = 1.5406Å) and Brag-Brentano optics configuration. A Cu-K_β filter was inserted to minimize the intensity of Cu-K_β x-ray. Wide range scans were performed at a step width of 0.01º and a speed of 4º/minute, while small range scans used a step width of 0.01º and a speed of 1º/minute. Once the peaks from the specimen were obtained, PDXL cards from International Centre for Diffraction Data (ICDD) were loaded to match the phases in the specimen.

2.2.3 Scanning Electron Microscope (SEM)

SEM has outperformed optical microscope in the materials imaging and characterization, as the resolution and magnification of the optical microscope are limited the wavelength of light. SEM uses a focused beam of electrons to bombard specimen, creating an interaction volume that contains signals of secondary electrons (SE), backscattered electrons (BSE), cathodoluminescence

(CL), continuum x-ray radiation, characteristic x-ray radiation and heat. Each signal is responsible for a specific information about the specimen.

FEI Magellan 400 XHR SEM (FEI, Eindhoven, The Netherlands) was used. To capture a high-resolution image of the specimen's surface topography, low voltage (5 kV) and low current (0.2 nA) with a through-the-lens detector (TLD) or Everhart-Thornley detector (ETD) were implemented, so only SE with low energy ($E < 50$ eV) generated near the specimen's surface would get detected. Even though both detectors could pick up BSE signal, the resolution was poor (Fig. 2.8). A concentric backscatter electron detector (CBS) was used along with high voltage (25 kV) and low current (0.2 nA) to collect information about phase distribution in the specimen. Contrast in phases is determined by the atomic number (Z) of the phases; phases with higher Z would appear brighter on BSE image, because more incident electrons would get scattered back to the detector. Energy dispersive spectroscopy (EDS) was used in conjunction with BSE to identify and quantify the elements in the specimen's phases. The voltage used for EDS was determined by the highest K_α among the phases' elements in interest. A rule of thumb was that a voltage of 1.5 times the highest K_α was used.

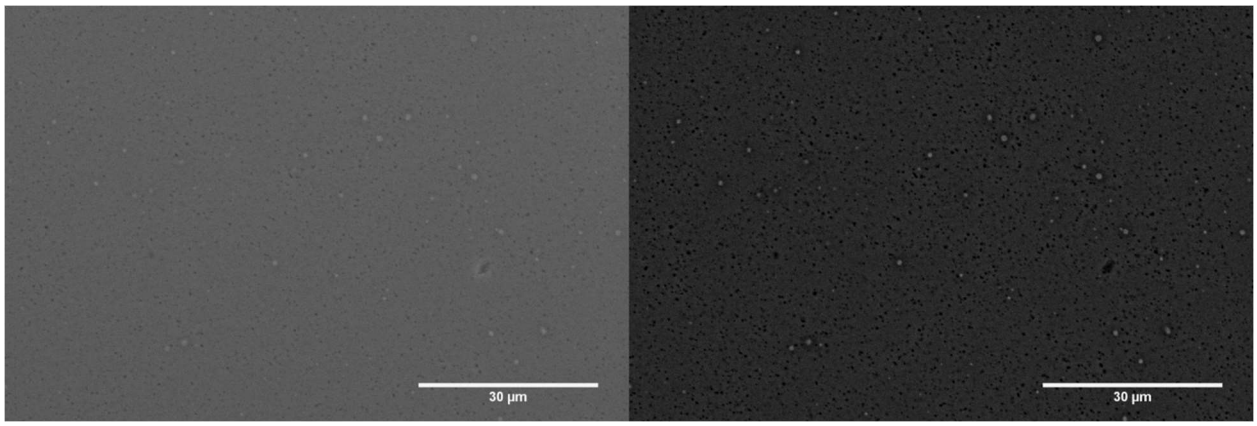

Figure 2.8: SE image (left) vs. BSE image (right)

CHAPTER 3: EFFECT OF WATER VAPOR ON THE DENSIFICATION OF OXIDES

3.1 Introduction

The capability of sintering oxides to nearly full density with lower sintering temperature and shorter sintering time would significantly reduce the cost for ceramic processing companies. The application of pressure during sintering process has proved to assist in faster densification of oxides. One may wonder whether other factors would also have the same effect, such as humid atmosphere.

Many researchers have reported enhanced sintering of oxides under humid atmosphere. Petersen et al. and Eastman et al. [3-4] have found faster densification rate of CaO and MgO, respectively, in the initial stage of sintering in humidified air. Their works showed that water vapor partial pressure was directly proportional to densification rate of the oxides (Fig. 3.1). A similar result was reported by Slodczyk et al. for Yb-substituted strontium zirconate (Yb:SZ) ceramic material [8]. Presence of hydroxyl group on Yb:SZ was observed in Raman and IR. The latest published article by Dargatz et al. also showed that full densification of ZnO could be attained at lower temperature when water was still effectively adsorbed on ZnO surface [5-7].

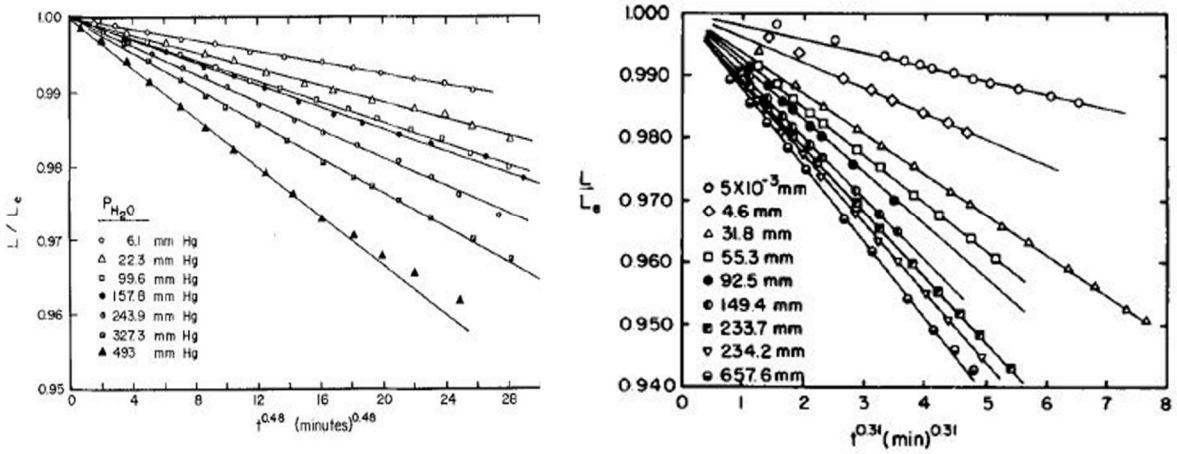

Figure 3.1: Initial stage of densification rate at several partial pressures of water vapor for CaO (left) and MgO (right) [3-4]

Alumina and 8YSZ are of technological importance for structural applications because of their superior mechanical properties. However, mechanical strength of ceramic materials is greatly reduced if the ceramics are not sintered to full density. In this experiment, we are investigating the effect of water vapor on sintering of these two materials. Spinel was also studied. Density after isothermal sintering at different temperatures is measured and compared between dry and humid air.

3.2 Experimental Procedures

Taimei α-alumina powder, Baikowski α-alumina powder, Baikowski spinel powder and Tosoh 8YSZ powder were ground with mortar and pestle to break down any agglomerates. Powders were cold isostatic pressed, and the green bodies were subjected in either dry or humid air in the tube furnace with an air flow rate of 50 cm^3/min. Water bath temperature was maintained at 60ºC, which was equivalent to a water vapor partial pressure of 0.2 atm. One trial was conducted at a higher water vapor partial pressure (0.52 atm) for Taimei α-alumina. Furnace temperature was first raised from room temperature to 300°C at a rate of 4.5°C/min and held for 10 hours. Then, the temperature was raised at a rate of 3°C/min to sintering temperatures. Isothermal sintering was conducted for 3 hours at temperatures ranging from 1000°C-1500°C. Each sintering run had four specimens in order to collect representative statistics. Density of sintered bodies was measured by following ASTM C20 described earlier.

3.3 Results and Discussion

Fig. 3.2 and 3.3 show that for both Baikowski α-alumina and spinel, it is observed that sintering occurs somewhere between 1100°C and 1200°C in both dry air and humid air. The comparison of average % theoretical density of sintered bodies between air and water vapor from 1200°C to 1500°C shows that there is no conspicuous increase of densification in water vapor for both materials (Fig. 3.4 and 3.5). On the other hand, finer powders of Taimei α-alumina and Tosoh 8YSZ show a slightly lower density for specimens sintered in humid air (Fig. 3.6 and 3.7). For Taimei α-alumina sintered at 1100°C, a trend of decreasing sintered density with increasing water vapor partial pressure is observed (Fig. 3.8).

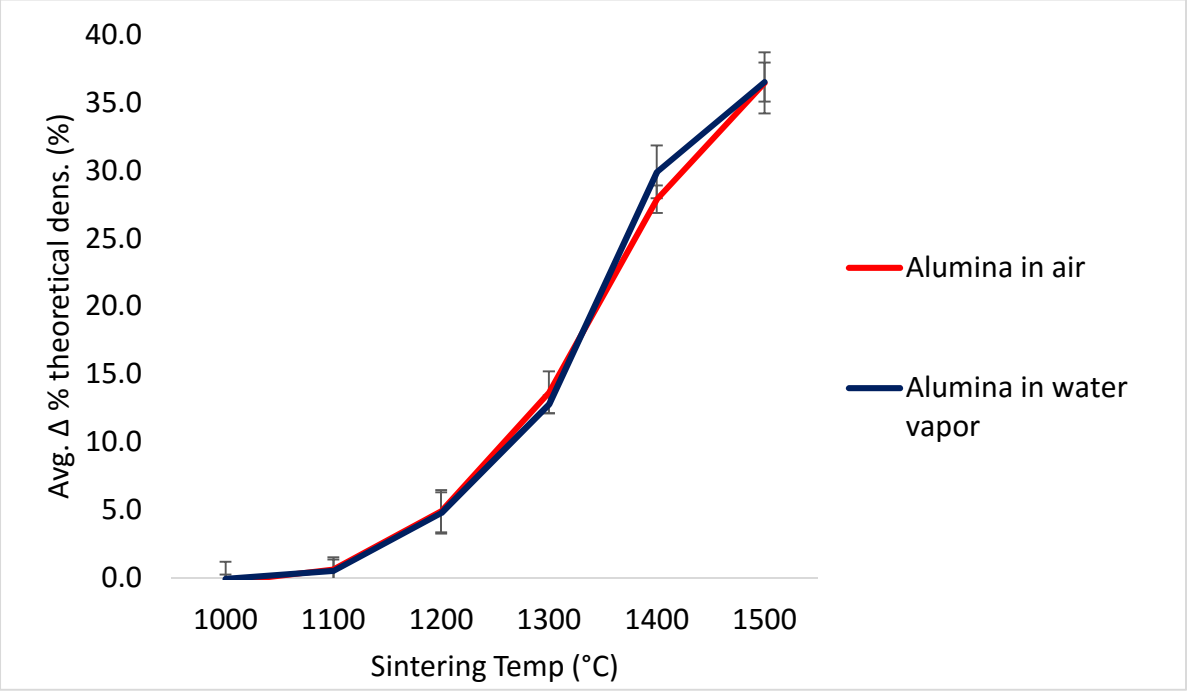

Figure 3.2: Sintering temperature vs. average change in % theoretical density of ground α-alumina in dry air vs. humid air

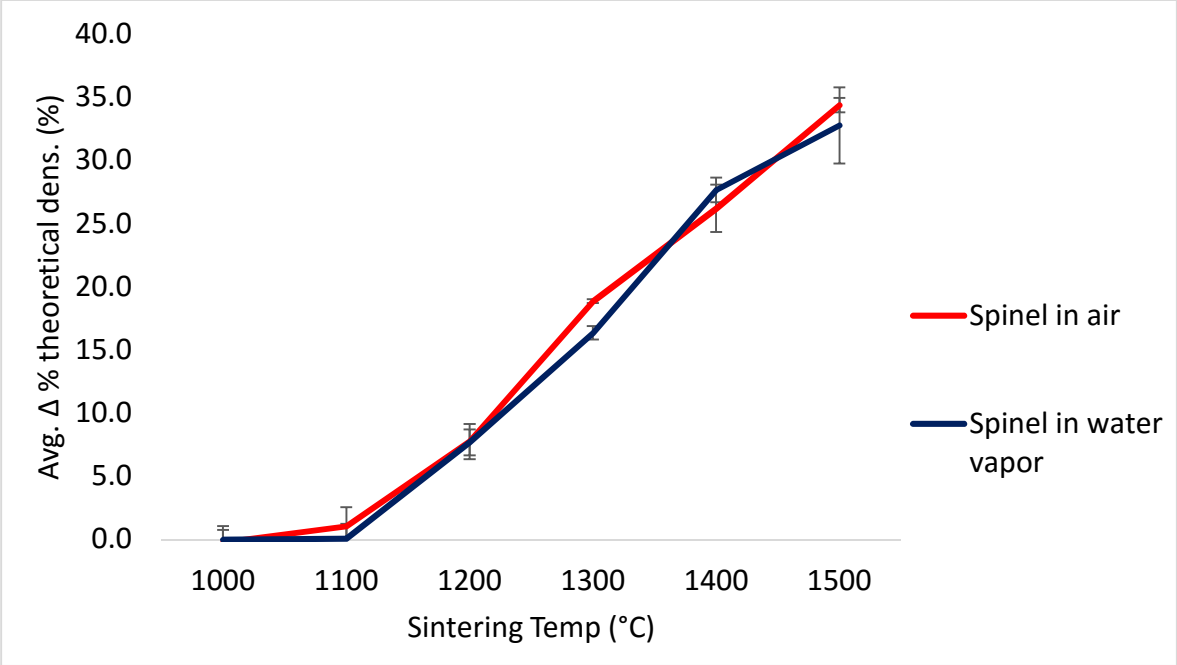

Figure 3.3: Sintering temperature vs. average change in % theoretical density of ground spinel in dry air vs. humid air

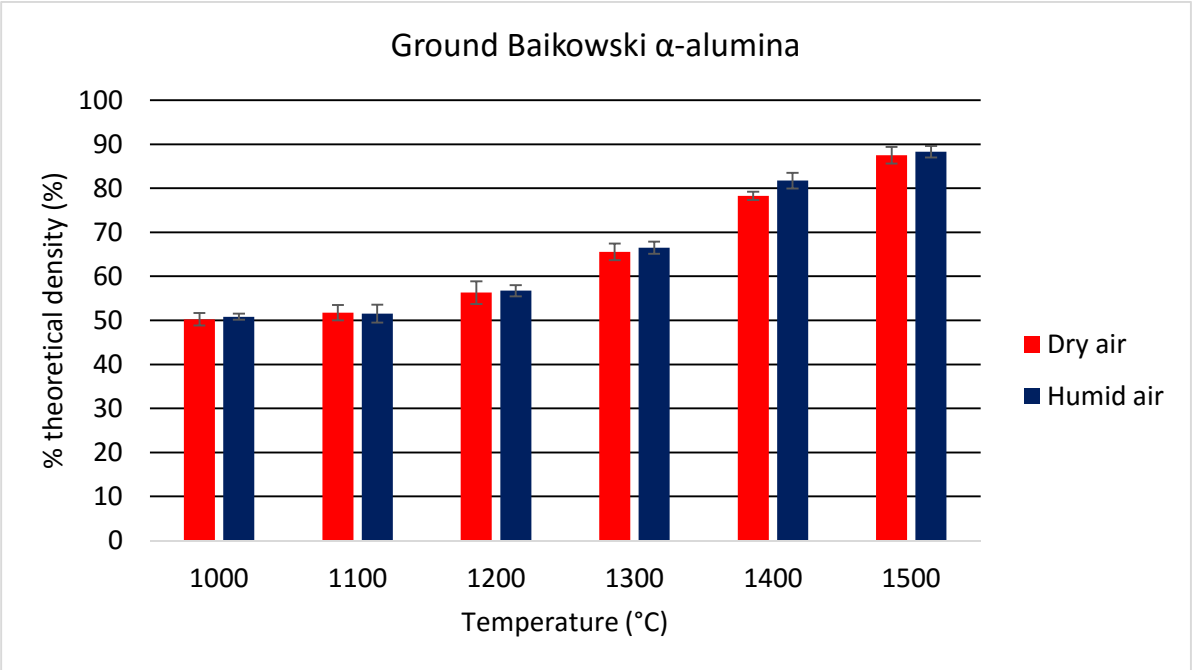

Figure 3.4: Average % theoretical density of sintered α-alumina in dry air vs. humid air at different sintering temperatures

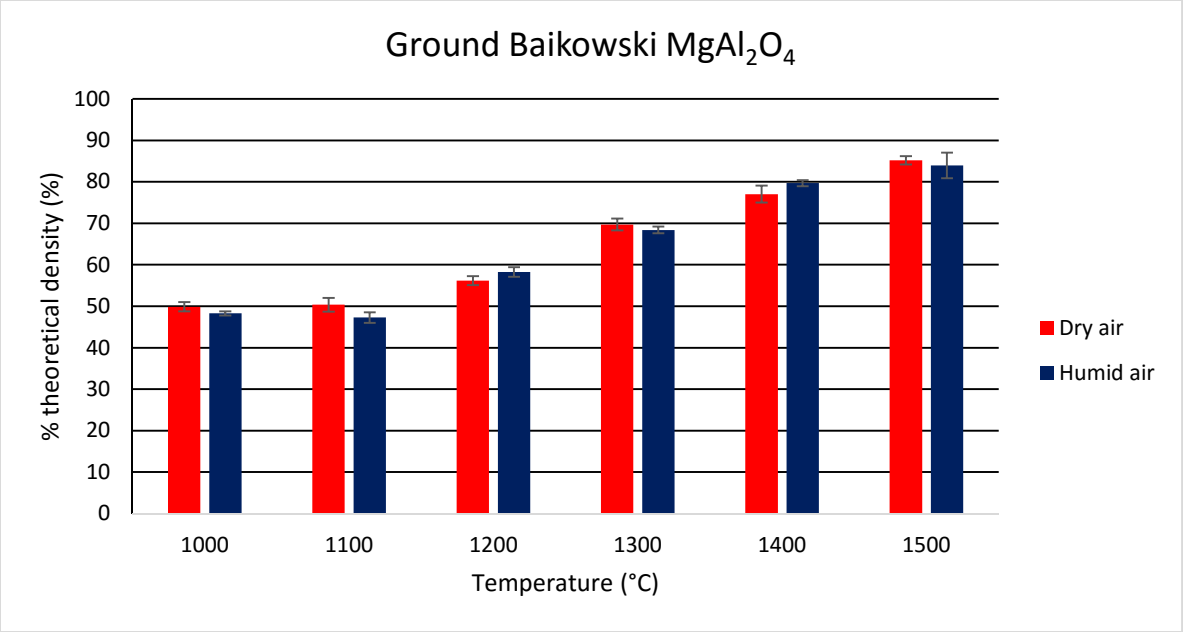

Figure 3.5: Average % theoretical density of sintered spinel in dry air vs. humid air at different sintering temperatures

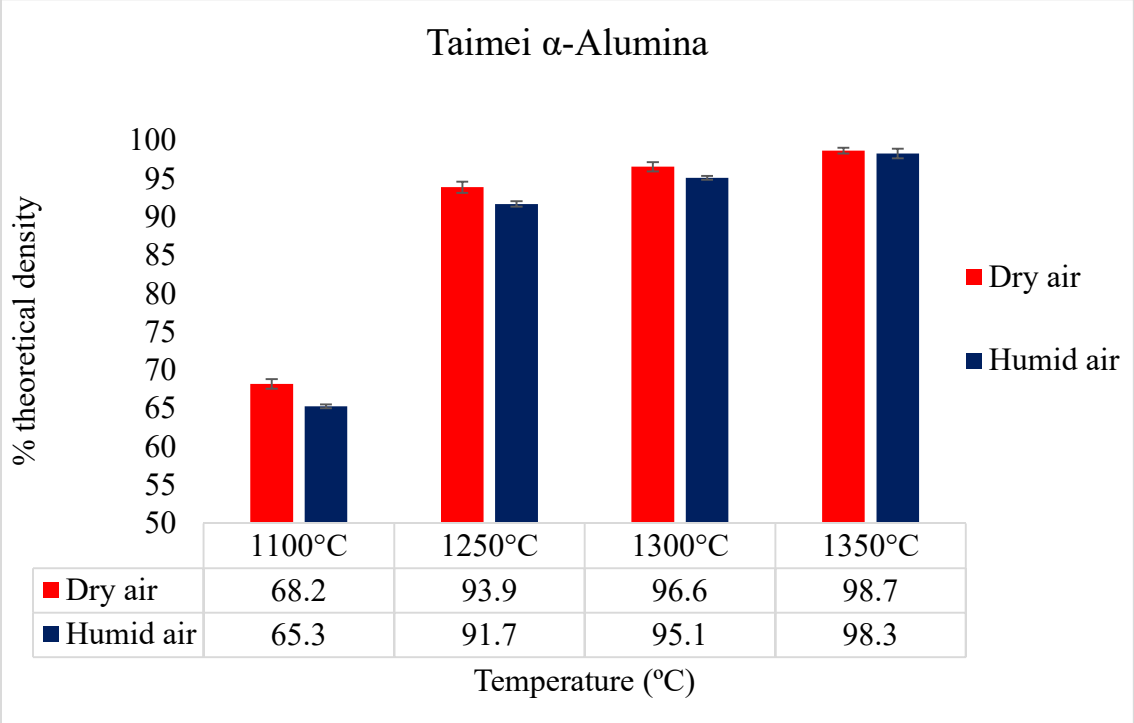

	1100°C	1250°C	1300°C	1350°C
Dry air	68.2	93.9	96.6	98.7
Humid air	65.3	91.7	95.1	98.3

Figure 3.6: Average % theoretical density of sintered Taimei α-alumina in dry air vs. humid air at different sintering temperatures

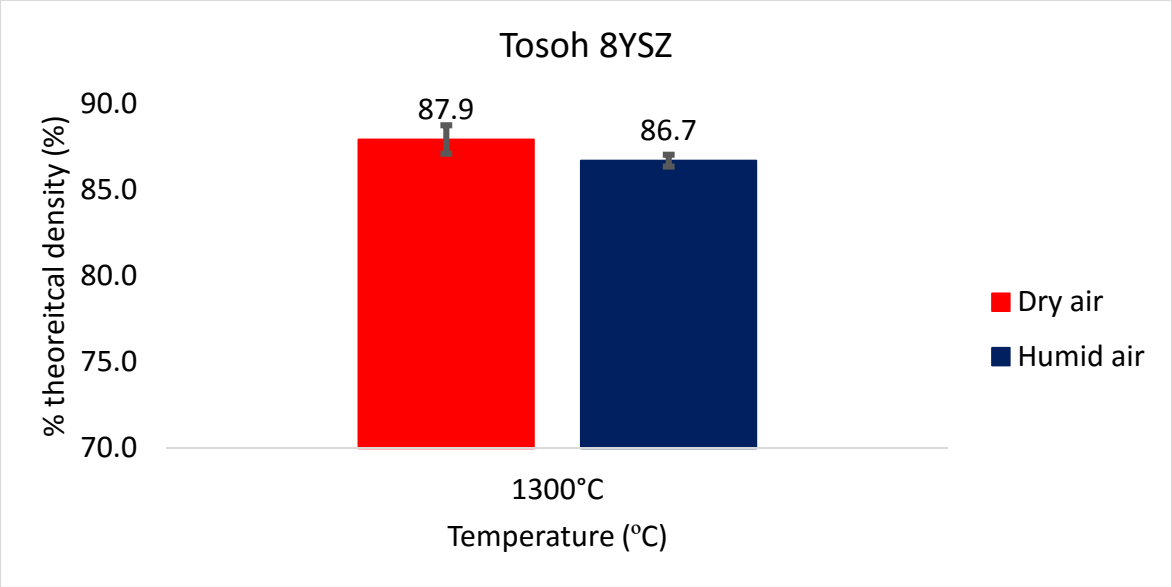

Figure 3.7: Average % theoretical density of sintered 8YSZ in dry air vs. humid air at 1300°C

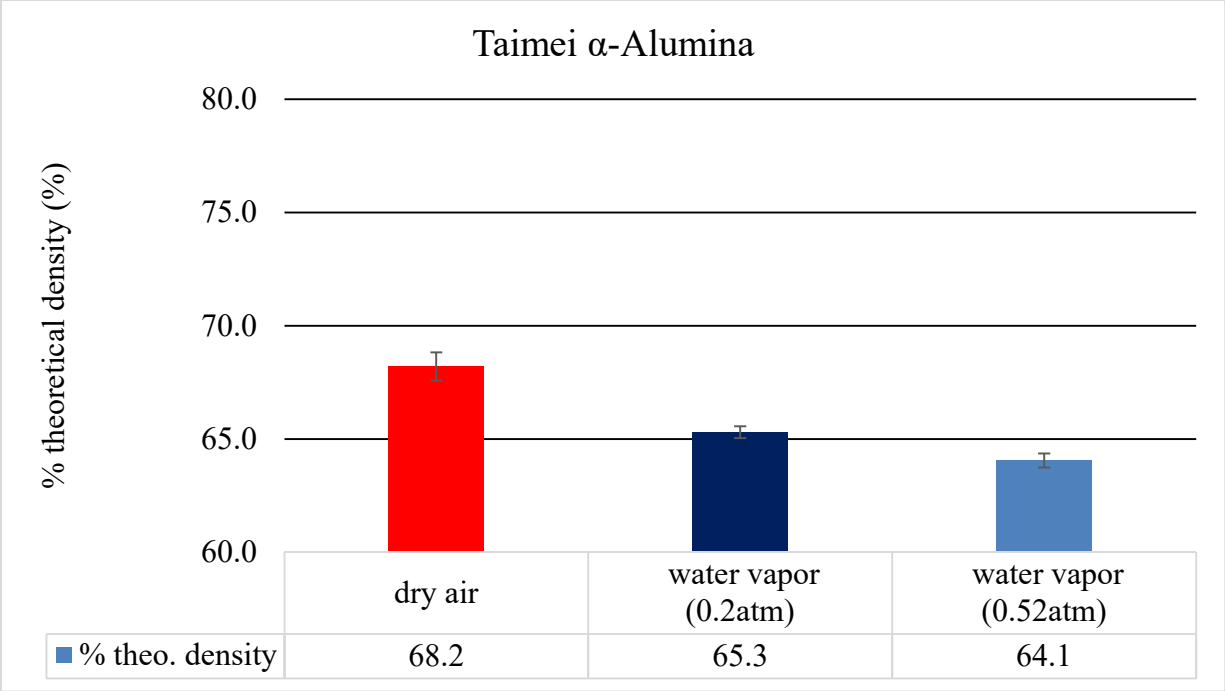

Figure 3.8: Average % theoretical density of sintered Taimei α-alumina in dry air vs. humid air at 1100°C with two different water vapor partial pressures

Possible explanation for the contradiction of what we are expecting is the enhanced surface diffusion in the presence of water vapor. Slow heating rate favors surface diffusion, since its activation energy is lower than that for grain-boundary diffusion. It is well understood that grain coarsening occurs through surface diffusion, and primary mechanism for sintering is grain-boundary diffusion. Therefore, with slow heating rate, the oxides spend more time coarsening before they start densifying regardless of whether they are sintered in dry air or humid air. With that being said, it appears that exacerbated coarsening in the presence of water vapor is due to the lowering of surface diffusion's activation energy and increase in grain boundary mobility by adsorbed water on the oxides' surface [9-10]. Moreover, it is very likely that water hardly participates in the densification of oxides, as holding the temperature at 300ºC and ramping temperature up slowly allow sufficient time for water to desorb from the oxides' surface. Dargatz et al. have proposed and experimented with fast heating rate to circumvent both complete water desorption at high temperature and grain coarsening at low temperature [6].

3.4 Conclusion and Future Work

Contrary to the hypothesis, no enhanced densification was found in the presence of water vapor. It is unclear whether water has played a role in non-densifying diffusion mechanisms such as surface diffusion, and thus, has resulted in lower sintered density. A new proposal for experimental procedure has been drafted. First, since the as-received powders have already been exposed to some extent of moisture, it is necessary to dry the powders in a desiccator before sintering in dry air. Moreover, pre-condition specimens in humid environment for the humid sintering by flushing the tube furnace with water vapor before starting the furnace run. This way, temperature holding at 300°C is unnecessary, and time frame for water desorption becomes much narrower. Last but not least, use fast sintering rate to allow specimens to have only a short time in the low temperature domain for surface diffusion. SPS can be incorporated in this case.

CHAPTER 4: EFFECT OF WATER VAPOR ON THE OXIDATION OF NICKEL MARKER DISPERSED IN 8YSZ MATRIX

4.1. Introduction

YSZ is widely used in various applications. It is extensively employed for electrolyte in solid oxide fuel cell (SOFC) and oxygen conductor due to its property of high oxygen conductivity. Moreover, SOFC's anode is commonly made of YSZ and Ni, with Ni acting as an electronic conductor. YSZ's low thermal conductivity and superior thermal shock resistance also made it a suitable material for thermal barrier coating (TBC). The aforementioned applications are constantly exposed to atmospheric environment, and one of the major concerns is that how water can impact the intended functions of these applications since water vapor is ubiquitous in the atmosphere. Many have reported that enhanced oxygen diffusion in ceramics and metal alloys is observed under humid environment [11; 15-17].

The presented experiment follows the approach outlined by Angle et al. [11] to test whether water vapor increases oxygen diffusion in 8YSZ. The Ni particles are homogeneously embedded in a dense 8YSZ matrix, but with much less composition of Ni in this experiment than in the SOFC since the Ni serves as a marker in the experiment. The extent of oxygen diffusion in 8YSZ can be gauged by the oxidation of Ni in dry and humid oxidizing environments at elevated temperature. The oxidation steps are the following in order: adsorption of oxygen gas on 8YSZ surface, decomposition of the O_2 to O atom, diffusion of the O atom through 8YSZ grain boundary to 8YSZ/Ni interface, and reaction between Ni and O to form NiO. It is assumed that the diffusion of the oxygen is the slowest step out of the four steps, and hence, it is the rate-limiting step for Ni oxidation.

4.2. Experimental Procedures

35 g of TZ-8ys powder was attrition-milled with 1.2 L of isopropanol and 750 g of 5 mm diameter YTZ grinding media (Tosoh) for 24 hours. The powder was then dried, ground and sieved. Milled 8YSZ powder and nickel oxide powder (Alfa Aesar) were ball-milled for 8 hours, dried, ground and sieved. The resulting powder mixture was heated at a rate of 3°C/min to 700°C, and maintained at 700°C for 10 hours in 4% H_2-Ar gas at a flow rate of 50 cm^3/min to reduce NiO to 0.5 vol% elemental Ni. The reduced Ni and 8YSZ mixture was ground, and then cylindrical specimens were prepared by cold isostatic pressing. Furnace temperature was first raised from room temperature to 300°C at a rate of 4.5°C/min and held for 5 hours. Then, the temperature was raised at a rate of 3°C/min to sintering temperatures of 1400°C, and held there for 5 hours in reducing atmosphere with a flow rate of 50 cm^3/min to sinter the specimens. Density was measured by ASTM C20 method. Sintered specimens were polished to a 0.1-micron finish. Polished surfaces were exposed to dry air or humid air (0.38 atm P_{water}) in the tube furnace. The temperature was first raised at a rate of 4.5°C/min and held at 300°C for 5 hours before raising the temperature at a rate of 10°C/min and oxidizing the specimens at 1000°C for times of 0.5, 1, 1.5 and 2 hours. Cross-sectioned specimens were cut from the oxidized specimens and polished down to 0.1-micron finish for imaging analysis.

Specimens were analyzed using Scanning electron microscopy (SEM) with energy dispersive spectroscopy (EDS) on a Magellan 400 (FEI, Eindhoven, The Netherlands), and X-ray diffraction (XRD) with a SmartLab X-ray Diffractometer (Rigaku, Tokyo, Japan) with Cu-K_α radiation. XRD data was obtained at a scan speed of 4°/minute in the range of 25-65°, and a scan speed of 1°/minute in the range of 42-46°. Backscattering electron imaging was used to reveal the oxidation boundary of nickel. The average oxidation depth measurement was done by ImageJ

(National Institutes of Health) on BSE images. 10 measurements in increment of 100 microns were measured to get a representative data on 1 mm along the edge of the polished surface.

4.3. Results and Discussion

The appearance of starting powder mixture of 8YSZ (white) and NiO (green) is white due to the tiny amount of NiO added. The powder turns gray-black after reduction, and remains the same color when the reduced powder is sintered. The gray-black color comes from the metallic color of nickel. Subsequent oxidations of the reduced specimens change the specimens' color from the surface slowly to the inner core from gray-black to lightly tan (Fig. 4.1). It is later discovered that the tan color is likely the result of Ni^{2+} solid solubility in 8YSZ [18]. Compared to Angle's oxidation of Ni in Al_2O_3 at 1300°C for 5 hours or more, Ni oxidation in 8YSZ is faster even at lower temperature for a short time (Fig. 4.1e) because oxygen diffusion is faster in 8YSZ [11].

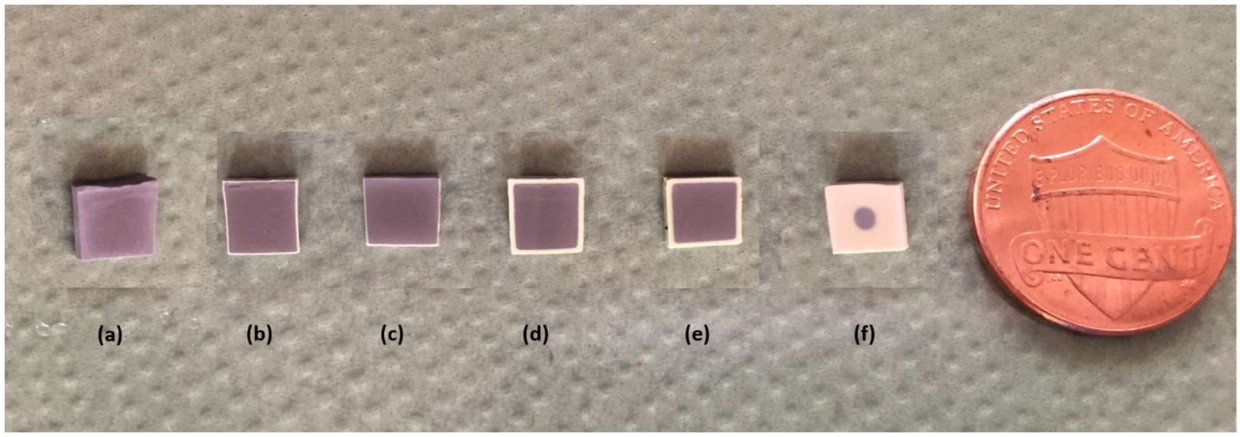

Figure 4.1: (a) Sinter reduced specimen; (b) Specimen oxidized in humid air at 900°C for 5 hours; (c) Specimen oxidized in dry air at 900°C for 5 hours; (d) Specimen oxidized in humid air at 1100°C for 3 hours; (e) Specimen oxidized in dry air at 1100°C for 3 hours; (f) Specimen oxidized in dry air at 1400°C for 1 hour

Density of the sintered 8YSZ/0.5 vol% Ni is measured consistently to be 97-98% of the theoretical density (5.92 g/cm^3) calculated from the rule of mixture equation (Equation 7).

$$\rho_{cermet} = \rho_{8YSZ}V_{8Y} + \rho_{Ni}V_{Ni} \qquad (7)$$

Starting density of 97-98% for the oxidation study is considered extremely high, as conventional sintering technique cannot achieve full density of ceramic materials. Nickel particles are seen

homogeneously distributed throughout the 8YSZ matrix before the specimen is oxidized (Fig. 4.2). Figure 4.3 shows that the reduced nickel particles are generally located at 8YSZ grain boundaries, because the free energy for reduction of NiO is lower at grain boundaries than in the bulk [19].

Figure 4.2: Nickel homogeneously distributed in 8YSZ matrix in BSE image

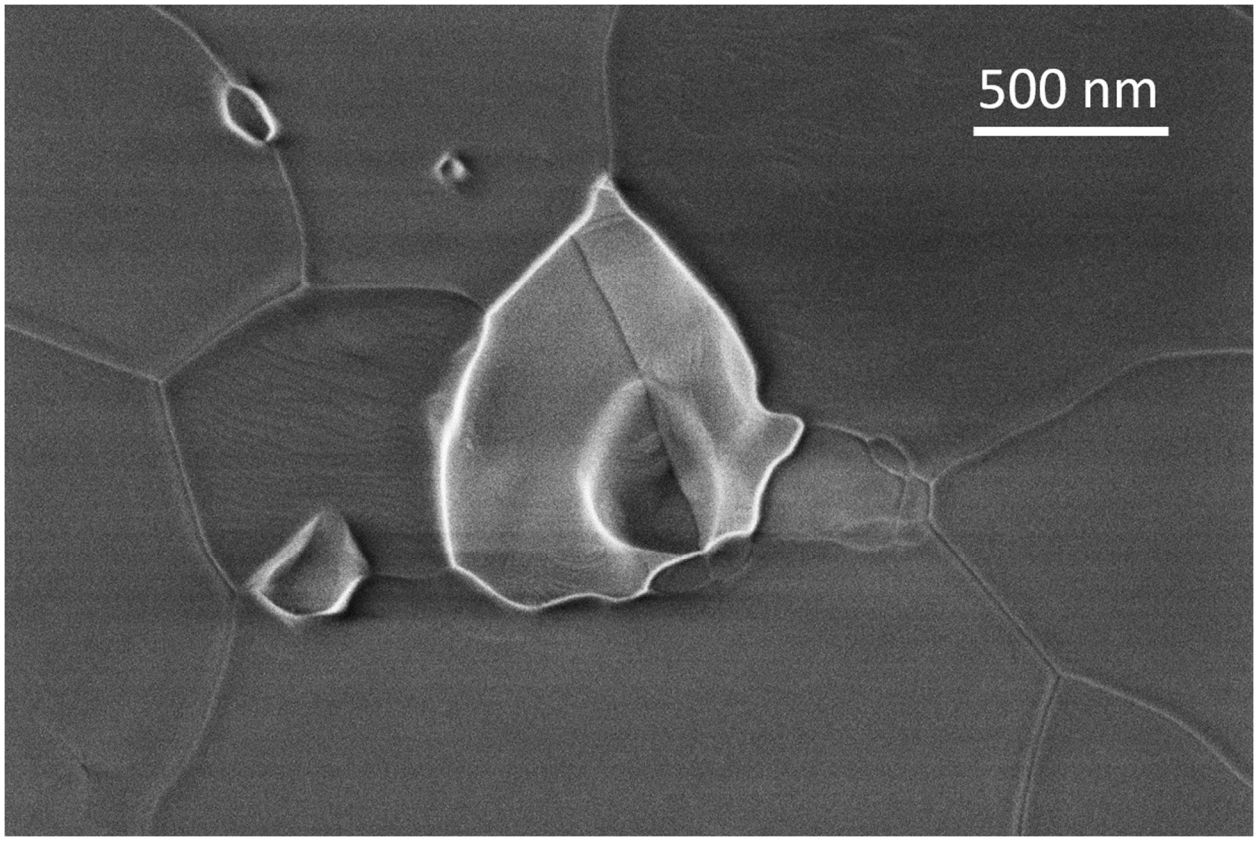

Figure 4.3: SE image showing a Ni particle located at 8YSZ grain boundary

During the reduction of the initial powder mixture of 8YSZ and NiO, 8YSZ remains the same phase, but NiO transform to Ni through the following reaction:

$$NiO\ (s) + H_2\ (g) \rightarrow Ni + H_2O\ (g)$$

The disappearance of NiO and the formation of Ni during the initial reduction can be seen in the XRD (Fig. 4.4). The sintered specimens retain Ni metal. When the specimens are oxidized, Ni peak disappears near the oxidized surface scanned by the XRD, but the reappearance of NiO is not observed (Fig. 4.4). No new peaks are formed, but all of the 8YSZ peaks are consistently shifted to higher 2θ, suggesting that there is NiO solid solution (Fig. 4.5). Solid solubility of NiO in YSZ depends on both temperature and Y_2O_3 content [20]. It is reported that a maximum solubility of 2.5 mol% of NiO in 8YSZ can be achieved by replacing Zr^{4+} lattice sites with Ni^{2+} [18]. The ionic radii for 6-fold coordinated Zr^{4+} and Ni^{2+} are 0.72 Å and 0.69 Å, respectively. Due to the nature of smaller ionic size of Ni, the displacement of the diffraction peaks to higher angle corresponds to a decreased lattice parameter for cubic 8YSZ in agreement with the finding from other studies [21-22]. In our study, 0.5 vol% Ni is equivalent to 1.67 mol% NiO in the 8YSZ matrix, which is below the solid solubility limit of NiO in bulk 8YSZ. Based on Table 4.1 from the XRD data, lattice parameter of 8YSZ changes from 5.1399 Å to 5.0817 Å after the dissolution of Ni in 8YSZ. The percent changes of the lattice parameter and the ionic radius are 1.1% and 4.2%, respectively. As it is expected, the lattice parameter changes in a smaller extent compared to the change of the ionic radius because only a few Zr^{4+} is replaced with Ni^{2+}. The formation of Ni solid solution can be described by the following reaction:

$$NiO \xrightarrow{8YSZ} V_{\ddot{O}} + O_O + Ni''_{Zr}$$

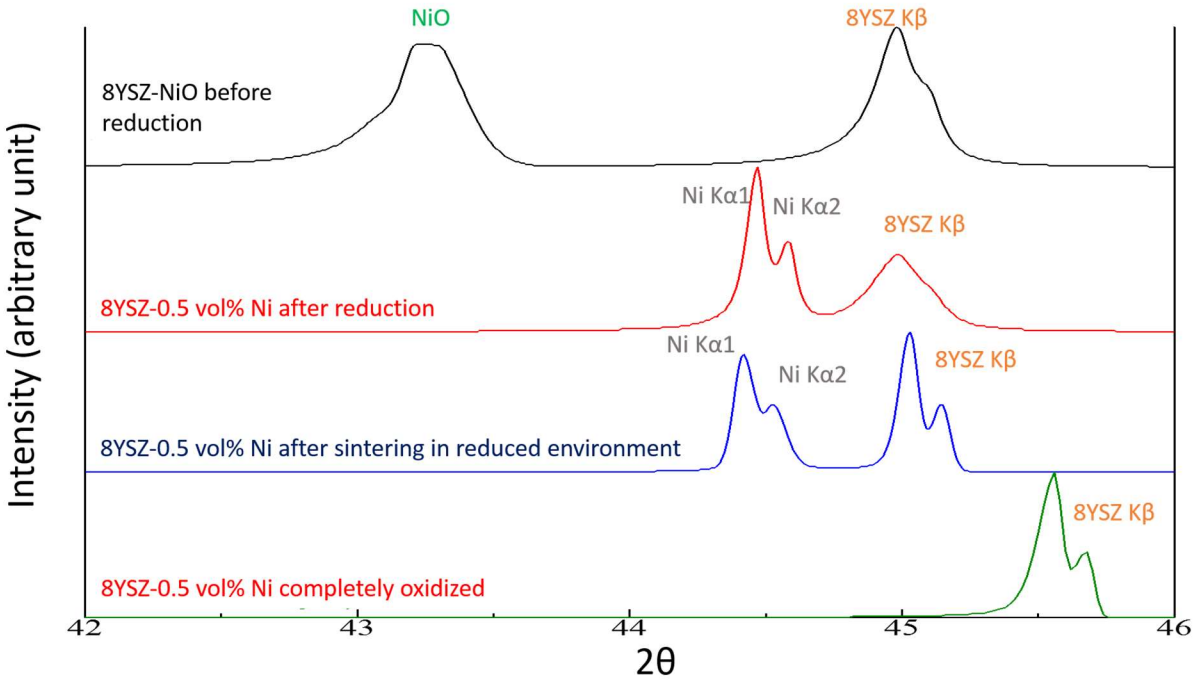

Figure 4.4: XRD data on specimen during each process

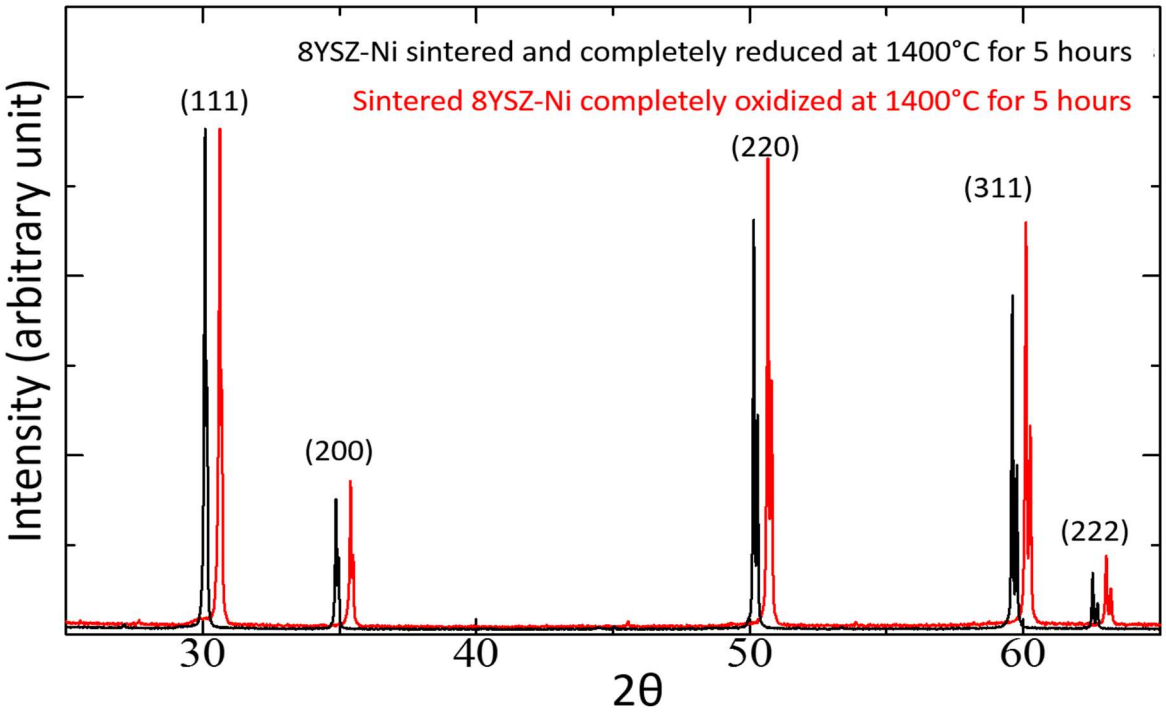

Figure 4.5: XRD on reduced sintered 8YSZ/Ni (black) and after its complete oxidation (red)

Table 4.1: XRD peak positions and their d-spacings of 8YSZ/Ni when reduced and oxidized

hkl (8YSZ)	8YSZ-Ni reduced		8YSZ-Ni oxidized	
Plane	2θ	d(Å)	2θ	d(Å)
1 1 1	30.09	2.97	30.61	2.92
2 0 0	34.88	2.57	35.41	2.53
2 2 0	50.16	1.82	50.67	1.80
3 1 1	59.61	1.55	60.10	1.54
2 2 2	62.55	1.48	63.03	1.47

The driving force for the inward diffusion of oxygen into 8YSZ/Ni is the difference in oxygen chemical potential between the surface and interior of the specimens by the induced air. Figure 4.6 uses BSE images to show the comparison of average Ni oxidation depths in dry and humid environments. The extent of oxygen grain-boundary diffusion can be evaluated by the depth of NiO dissolution in 8YSZ. The depth of oxidation is an averaged value between the end depth of formation of Ni solid solution in 8YSZ and the beginning depth of residual un-oxidized Ni particles. An increase of Ni oxidation depth for the same oxidizing time and temperature in the presence of water vapor is clearly shown in the BSE images. While it is clear that Ni metal particles appear bright under BSE mode, the contrast between Ni in solid solution and 8YSZ matrix is not obvious, and only with the use of EDS can we clearly see the distribution of Ni solid solution in 8YSZ (Fig. 4.7).

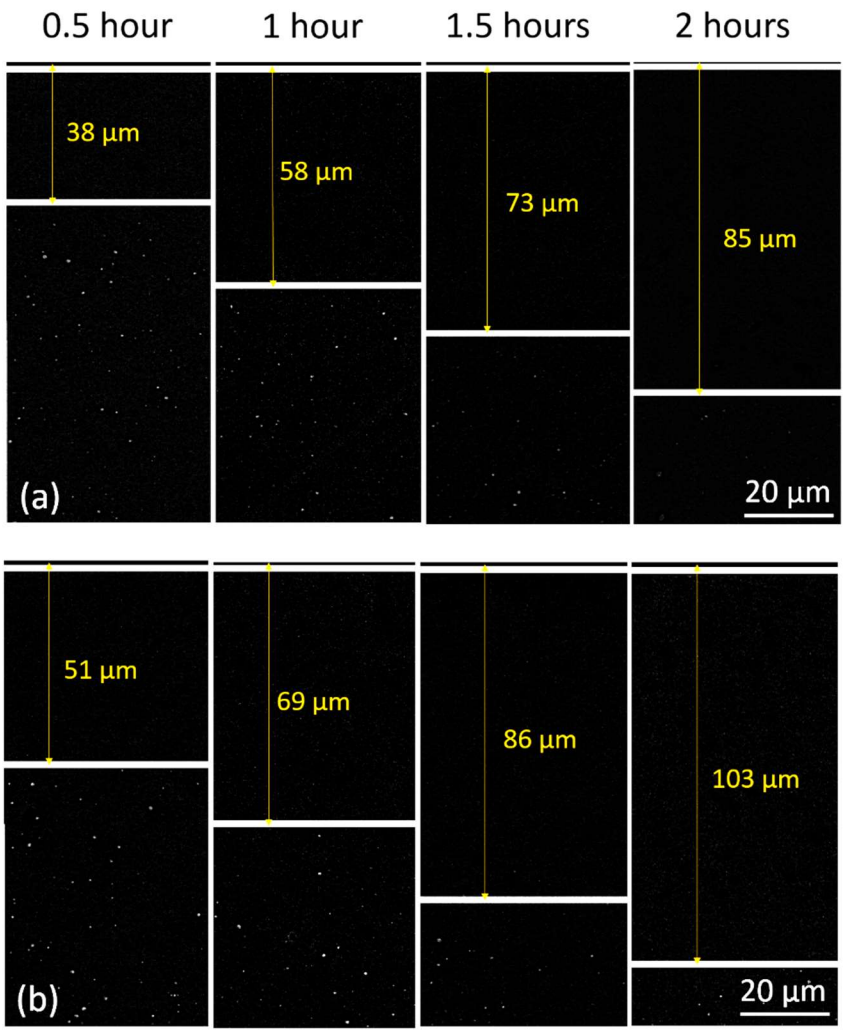

Figure 4.6: Average oxidation depth (x) from top free surface for the time periods of 0.5, 1, 1.5, and 2 hours at 1000°C under (a) dry and (b) humid atmospheres

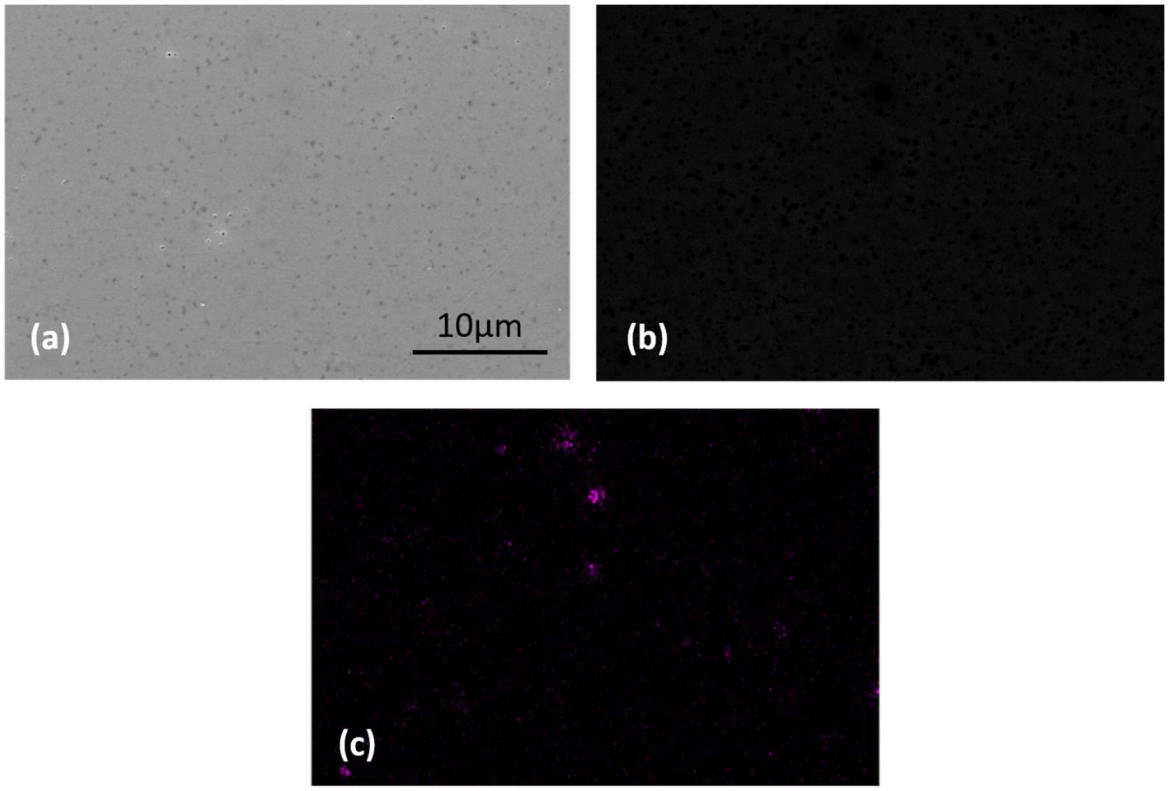

Figure 4.7: (a) SE image of a cross-sectioned oxidized specimen; (b) BSE image at the same area of the specimen; (c) EDS image of Ni signal at the same area of the specimen

Because the plot of average oxidation depth versus oxidizing time resembles a parabolic curve shown in Fig. 4.8, a parabolic rate law is adopted [11; 18]. The observed parabolic behavior suggests that the oxide growth is limited by diffusion and not by reaction, since diffusion-controlled reaction processes follow a parabolic relationship between time and oxide thickness. Fig. 4.9 plots the square of average oxidation depth against oxidizing time. The kinetic rate constants are determined by the slope of the fitted lines. The rate constants for dry oxidation (k_{dry}) and humid oxidation (k_{humid}) are 9.83 x 10^{-13} m^2/s and 1.41 x 10^{-12} m^2/s, respectively. It is shown that humid environment accelerates inward oxygen diffusion and subsequent oxidation of the Ni particles by 44%. The enhanced oxidation in 8YSZ (44%) is lower than that in Al_2O_3 (79%) because 8YSZ already has high oxygen diffusivity [11].

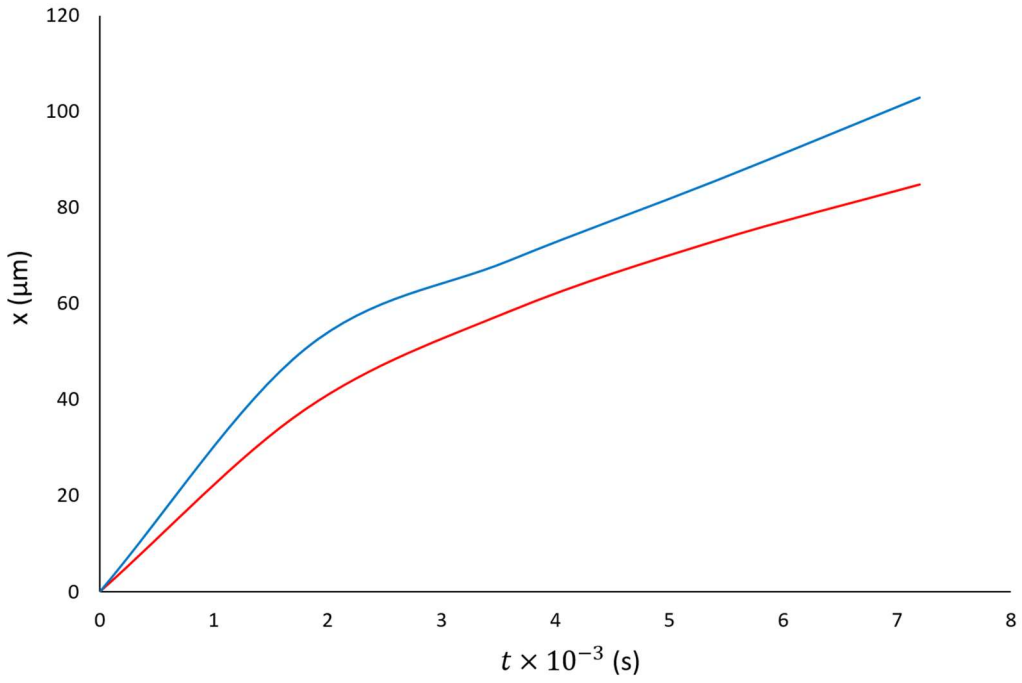

Figure 4.8: A parabolic relationship between time and oxidation depth under dry air (red) and humid air (blue)

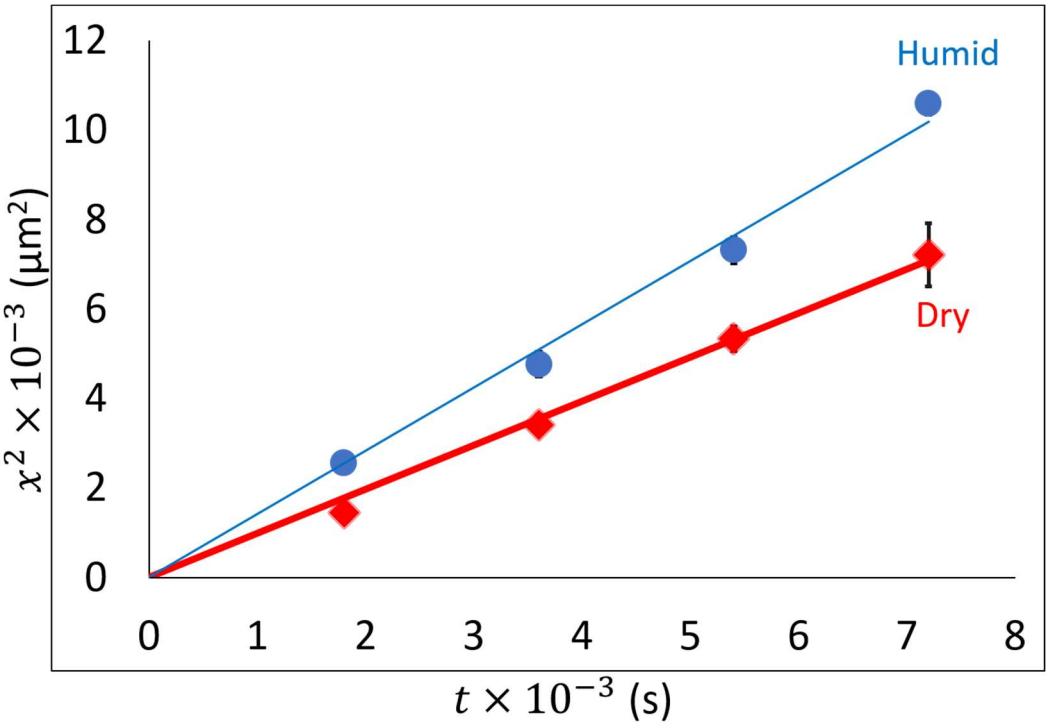

Figure 4.9: Square of the average oxidation depth vs. oxidation time under dry air (red) and humid air (blue)

The reason that 8YSZ is such a good oxygen conductor is that yttrium doping has resulted in the formation of oxygen vacancies, and these vacancies facilitate oxygen movement through vacancy diffusion. If the enhanced oxygen diffusion under the presence of water vapor is attributed to vacancy diffusion, it should mean that water vapor creates more oxygen vacancies. If the water dissociation mechanism described in equation 1 is correct, an oxygen vacancy is removed when water molecules dissociate onto oxide surface. In fact, surface oxygen vacancies are known to be occupied by hydroxyl ions when water molecules dissociate [12; 15-17; 23]. Therefore, it is unlikely that vacancy diffusion mechanism plays a role in the enhanced oxygen diffusion.

Easy diffusion path for oxygen grain-boundary diffusion can be achieved by the incorporation of protons from water. The protons can move in two different ways: transport of protons as hydroxyl ions, and jumping of protons between stationary oxygen ions. Researchers have suggested that oxygen ions in the form of hydroxides has faster surface diffusion than oxygen ions alone [17; 24]. Intuitively, one may speculate that the same phenomenon would hold true for hydroxyl ions diffusing along grain boundary based on inductive reasoning. The smaller size and reduced charge of hydroxyl ions compared to oxide ions help facilitate the oxygen grain-boundary diffusion [15; 25]. When transport as hydroxyl ions is energetically unfavorable, proton hopping can occur to overcome this barrier and further diffuse as hydroxides with neighboring oxygen ions, thus a proton-assisted accelerated oxygen diffusion [16].

While enhanced oxidation and oxygen diffusion under exposure to water vapor are known for a long time, researchers are still investigating the controlling mechanism to these phenomena. The proton-assisted accelerated oxygen grain-boundary diffusion in 8YSZ can be viewed as a simple, ideal interpretation. However, there are other factors that may contribute to

the enhanced oxygen diffusion. The presence of impurities in the material may also increase oxygen diffusion when exposed to water vapor, possibly by removing diffusion-inhibiting impurities from grain boundary [26]. It is also possible that yttrium ions, which are known to block oxygen ion diffusion along grain boundaries, are removed or mitigated by the presence of hydroxyl ions [2; 27].

4.4. Conclusion and Future Work

A cermet composite system is used to explore the effect of water vapor on the extent of nickel oxidation as a measure of oxygen diffusion in the system. Enhanced grain-boundary oxygen diffusion at high temperature humid environment in 8YSZ is observed, possibly due to the transport of oxygen ions as hydroxyl ions. It is believed that diffusion coefficient of hydroxyl ions is higher than that of oxygen ions because hydroxyl ions are 1) smaller in size and 2) less charged than oxygen ions. Alternatively, faster oxidation of Ni under humid environment can be explained by the lower activity/concentration of hydroxide required to react with Ni compared to that of oxygen. However, it is not known in this study. The study can be extended to the following:

1. Oxidation studies can be conducted at 900°C and 1100°C to determine the kinetic rate constants at these temperatures. The activation energies for oxygen diffusion in dry air and humid air can be determined by plotting natural log of these rate constants against inverse of the temperatures.
2. Since it is believed that the underlying mechanism of the observed phenomenon is grain-boundary oxygen diffusion, a range of grain sizes can be tested to corroborate the claim.
3. Isotopic oxygen (O^{18}) can be used for the same experiment. By implementing SIM and IR, isotopic oxygen and hydroxyl species can be traced.

Based on the observed result of enhanced oxygen diffusion in 8YSZ in the presence of water vapor, one may predict how moisture in the atmosphere can impact many applications where YSZ is used in high temperature. While the enhanced oxygen diffusion can be advantageous for SOFC and oxygen conductor, it is detrimental to TBC as the underlying metal will become vulnerable to oxygen corrosion.

4.5. Troubleshooting

The presented results come from the second set of the experiment, as the first data set has inconsistencies. Fig. 4.10 shows the first set of the dry oxidation at 1000°C. Compared to Fig. 4.6(a), the result in Fig. 4.10 is consistently higher by 50% for each oxidation time. The kinetic rate constant is determined to be 2.31 x 10^{-12} m^2/s (Fig. 4.11). The cause of the inconsistency is not yet found, but it is likely due to inaccurate reading of the thermocouple or gas leakage in the initial setup.

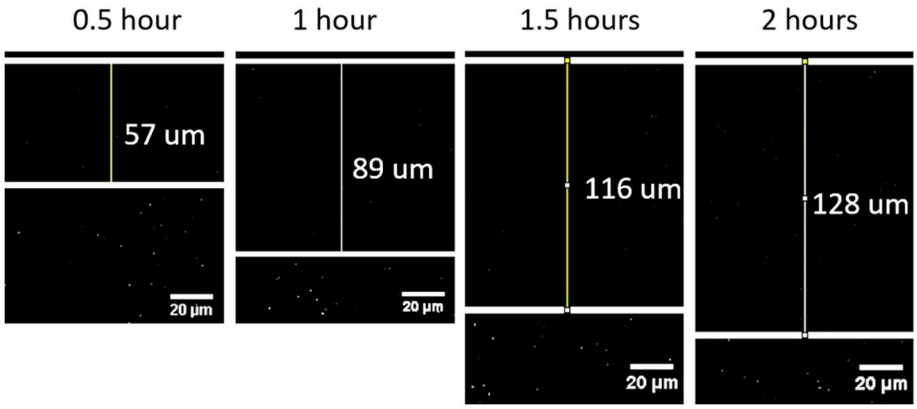

Figure 4.10: Average oxidation depth (x) from top free surface for the time periods of 0.5, 1, 1.5, and 2 hours at 1000°C in dry air (first set)

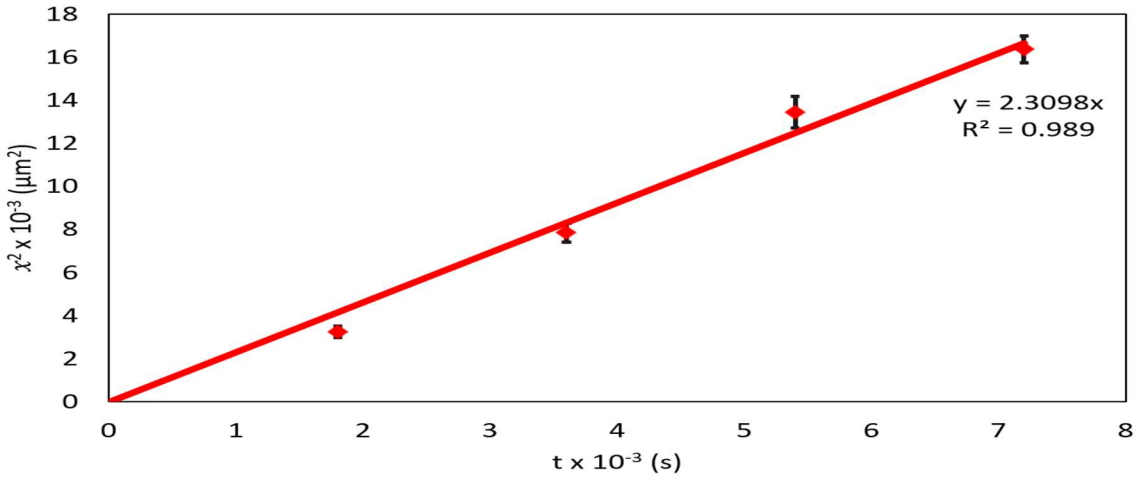

Figure 4.11: Square of the average oxidation depth vs. oxidation time under dry air (first set)

REFERENCES

1. Adil Saeed, Zulfiqar A. Khan, and Mian Hammad Nazir, "Time Dependent Surface Corrosion Analysis and Modelling of Automotive Steel under a Simplistic Model of Variations in Environmental Parameters." *Materials Chemistry and Physics*, 178 65-73 (2016).

2. Masahiro Yoshimura, Tatsuo Noma, Katsuichi Kawabata, and Shigeyuki Somiya, "Role of H_2O on the Degradation Process of Y-TZP." *Journal of Materials Science Letters*, 6**[4]** 465-67 (1987).

3. Paul F. Eastman, and Ivan B. Cutler, "Effect of Water Vapor on Initial Sintering of Magnesia." *Journal of the American Ceramic Society*, 49**[10]** 526-30 (1966).

4. Ronald O. Peterson, and Ivan B. Cutler, "Effects of Water Vapor on the Initial Sintering of Calcia." *Journal of the American Ceramic Society*, 51**[1]** 21-22 (1968).

5. Benjamin Dargatz, Jesus Gonzalez-Julian, and Olivier Guillon, "Effect of Electric Field and Atmosphere on the Processing of Nanocrystalline ZnO." *Oxide-based Materials and Devices V*, (2014).

6. Benjamin Dargatz, Jesus Gonzalez-Julian, Martin Bram, Peter Jakes, Astrid Besmehn, Lisa Schade, Robert Roder, Carsten Ronning, and Olivier Guillon, "FAST/SPS Sintering of Nanocrystalline Zinc Oxide-Part I: Enhanced Densification and Formation of Hydrogen-related Defects in Presence of Adsorbed Water." *Journal of the European Ceramic Society*, 36**[5]** 1207-220 (2016).

7. Benjamin Dargatz, Jesus Gonzalez-Julian, Martin Bram, Yutaka Shinoda, Fumihiro Wakai, and Olivier Guillon, "FAST/SPS Sintering of Nanocrystalline Zinc Oxide-Part II: Abnormal Grain Growth, Texture and Grain Anisotropy." *Journal of the European Ceramic Society*, 36**[5]** 1221-232 (2016).

8. Aneta Slodczyk, Olivier Lacroix, and Philippe Colomban, "Water Pressure Enhanced Sintering of Alkaline-earth Perovskite Ceramics." *Ceramics International*, 41**[9]** 11528-1533 (2015).

9. P.J. Anderson, and P. L. Morgan, "Effects of Water Vapour on Sintering of MgO." *Trans. Faraday Soc*., 60**[4975]** 930-7 (1964).

10. Roger B. Bagwell, and Gary L. Messing, "Effect of Seeding and Water Vapor on the Nucleation and Growth of α-Al_2O_3 from γ-Al_2O_3." *Journal of the American Ceramic Society*, 82**[4]** 825-32 (1999).

11. J. P. Angle, P. E. D. Morgan, and M. L. Mecartney, "Water Vapor-Enhanced Diffusion in Alumina." *J. Am. Ceram. Soc*., 96**[11]** 3372-374 (2013).

12. Matthias T. Elm, Jonas D. Hofmann, Christian Suchomski, Jurgen Janek, and Torsten Brezesinski, "Ionic Conductivity of Mesostructured Yttria-Stabilized Zirconia Thin Films with Cubic Pore Symmetry-On the Influence of Water on the Surface Oxygen Ion Transport." *ACS Appl. Mater. Interfaces*, 7**[22]** 11792-1801 (2015).

13. R. D. Shannon, "Revised Effective Ionic Radii and Systematic Studies of Interatomic Distances in Halides and Chalcogenides." *Acta Crystallogr. A*, 32**[5]** 751-67 (1976).

14. ASTM C20-00 (2015), Standard Test Methods for Apparent Porosity, Water Absorption, Apparent Specific Gravity, and Bulk Density of Burned Refractory Brick and Shapes by Boiling Water, ASTM International, West Conshohocken, PA, 2015.

15. S. Basu, N. Obando, A. Gowdy, I. Karaman, and M. Radovic, "Long-Term Oxidation of Ti_2AlC in Air and Water Vapor at 1000-1300°C Temperature Range." *J. Electrochem. Soc*., 159**[2]** C90-96 (2012).

16. S. R. J. Saunders, M. Monteiro, and F. Rizzo, "The Oxidation Behaviour of Metals and Alloys at High Temperatures in Atmospheres Containing Water Vapour: A Review." *Prog. Mater. Sci.*, 53**[5]** 775-837 (2008).

17. Fumihiki Kosaka, Hiroyuki Hatano, Yoshito Oshima, and Junichiro Otomo, "Iron Oxide Redox Reaction with Oxide Ion Conducting Supports for Hydrogen Production and Storage Systems." *Chemical Engineering Science*, 123 380-87 (2015).

18. Amy Morrissey, James R. O'brien, and Ivar E. Reimanis, "Tailored Metal-ceramic Nanocomposites Prepared by Redox Cycling of Polycrystalline Ni-doped Yttria Stabilized Zirconia." *Scripta Materialia*, 112 109-13 (2016).

19. Amy Morrissey, James R. O'brien, and Ivar E. Reimanis, "Microstructure Evolution during Internal Reduction of Polycrystalline Nickel-doped Yttria-stabilized Zirconia." *Acta Materialia*, 105 84-93 (2016).

20. Soren Primdahl, Bent F. Sorensen, and Mogens Mogensen, "Effect of Nickel Oxide/Yttria-Stabilized Zirconia Anode Precursor Sintering Temperature on the Properties of Solid Oxide Fuel Cells." *J. Am. Ceram. Soc*., 83**[3]** 489-94 (2000).

21. Josh White, Ivar E. Reimanis, Sophie Menzer, and Grover Coors, "The Enhanced Stabilization of the Cubic Phase in Yttria-Stabilized Zirconia with the Addition of Nickel Oxide." *J. Am. Ceram. Soc*., 94**[7]** 2030-036 (2011).

22. Soren Linderoth, Nikolaos Bonanos, Karin V. Jensen, and Jorgen B. Bilde-Sorensen, "Effect of NiO-to-Ni Transformation on Conductivity and Structure of Yttria-Stabilized ZrO_2." *J. Am. Ceram. Soc*., 84**[11]** 2652-656 (2001).

23. M. J. Pietrowski, R. A. De Souza, M. Fartmann, R. ter Veen, M. Martin, "Oxygen Isotope Transport Properties of Yttria-Stabilized Zirconia (YSZ) in O_2- and H_2O-Containing Atmospheres." *Fuel Cells*, 13**[5]** 673-81 (2013).

24. M. Pijolat, M. Dauzat, and M. Soustelle, "Influence of Water-Vapor and Additives on the Surface-Area Stability of γ-Al_2O_3." *Solid State Ionics*, 50**[1-2]** 31-9 (1992).

25. Truls Norby, "Protonic Defects in Oxides and Their Possible Role in High Temperature Oxidation." *Journal de Physique IV Colloque*, 3**[C9]**, 99-106 (1993).

26. S. Balcon, S. Mary, C. Kappenstein, and E. Gengembre, "Monopropellant Decomposition Catalysts II. Sintering Studies on Ir/Al_2O_3 Catalysts, Influence of Chloride Anions." *Appl. Catal. A*, 196**[2]** 179-90 (2000).

27. Huikai Cheng, Shen J. Dillon, Hugo S. Caram, Jeffrey M. Rickman, Helen M. Chan, and Martin P. Harmer, "The Effect of Yttrium on Oxygen Grain-Boundary Transport in Polycrystalline Alumina Measured Using Ni Marker Particles." *J. Am. Ceram. Soc*., 91**[6]** 2002-008 (2008).